Low-Dose Nanoscale Visualization of Crystal Phases in Epitaxial Cathodes via Cepstral Matching of Scanning Nanobeam Electron Diffraction

Kohei Aso[1], Takafumi Kakeya[1], Takumu Tsuchida[1], Hiroki Ito[2], Sho Asano[2], Kenta Watanabe[2], Kazutaka Mitsuishi[3], Koji Kimoto[3], Keisuke Shinoda[3], Takuya Masuda[3*], Masaaki Hirayama[2*], and Yoshifumi Oshima[1*]

1 Japan Advanced Institute of Science and Technology, Ishikawa, 923-1292, Japan

2 Institute of Science Tokyo, Kanagawa 226-8501, Japan

3 National Institute for Materials Science, Ibaraki, 305-0044, Japan

*Corresponding authors

TM: MASUDA.Takuya@nims.go.jp

MH: hirayama@mct.isct.ac.jp

YO: oshima@jaist.ac.jp

ABSTRACT (149 words)

Layered cathodes are essential for achieving a high energy density in rechargeable lithium-ion batteries, but they suffer from capacity fade due to local crystal phase transitions during charge–discharge cycles. Understanding these phase transitions is essential to minimizing their effects, but their nanometer size and sensitivity to experimental conditions make observation difficult. Here, we visualized nanometer-scale crystal phases within an epitaxial $LiCoO_2$

cathode after 100 charge–discharge cycles by matching experimental and simulated cepstra derived from scanning nanobeam electron diffraction. While the $LiCoO_2$ bulk remained a layered structure, spinel- and rock salt-type phases were observed within 3 nm of the cathode–electrolyte interface. The developed method achieved a spatial resolution of 1.5 nm across a field of view of several hundred nanometers with minimal electron beam damage. The cepstral matching analysis offers valuable insights into the interfacial phase transitions and will aid in the design of high-performance lithium-ion batteries.

KEYWORDS

Lithium-ion batteries, $LiCoO_2$ cathodes, Epitaxial film, Nanoscale crystal-phase mapping, Cepstral matching analysis, Scanning nanobeam electron diffraction

MAIN (3160 words excluding Figure captions)

Rechargeable lithium-ion batteries (LIBs) are representative energy storage devices owing to their efficient energy utilization.[1,2] Layered cathodes, comprising a stack of alternating (003) layers of lithium (Li) with a transition metal oxide, are one of the promising cathode materials to achieve high energy density LIBs.[3] Lithium cobalt oxide ($LiCoO_2$) is a typical layered cathode and has a theoretical capacity of 274 mAh g^{-1} at a charging voltage of ~4.8 V (vs. Li/Li^+).[4] However, LIBs that combine a $LiCoO_2$ cathode with a liquid electrolyte are limited to a capacity of ~140 mAh g^{-1} to ensure a stable charge–discharge cycle.[1,2,5,6] One reason for the limitation is that charging at voltages above 4.2 V triggers the crystal phase transitions into spinel-type[6–13] and rock salt-type phases[10–14] of the cathode after several charge–discharge

cycles. These phase transitions cause cobalt (Co) ions to migrate to the pristine Li layers, which results in poor Li-ion conductivity, and their irreversibility results in capacity fade. These interfacial phase transitions can propagate several nanometers into the cathode from the cathode–electrolyte interface, underscoring the need for nanoscale characterization to develop LIBs with higher energy density and longer cycle life.

Meanwhile, conventional cathodes are often composites of particles that are several micrometers in size. However, the random crystal orientations of these particles make it difficult to understand such phase transitions. In addition, the lattice constant along the *c*-axis changes depending on the Li-ion concentration, which results in inhomogeneous changes in volume during charge–discharge cycles that can lead to cracks. This mechanical degradation further complicates the analysis of phenomena that take place at the cathode–electrolyte interface. In contrast, epitaxial cathodes offer controlled orientation through the substrate and consist of much smaller domains with only a few tens to hundreds of nanometers in size, which reduces the volumetric change during charge–discharge cycles and thus minimizes cracks. Therefore, the epitaxial cathode provides a simplified interface to understand the structural and compositional change caused by Li-ion intercalation/deintercalation during the cycle.[12,13,15–20]

Ito et al.[17] used grazing-incidence X-ray diffraction to investigate structural changes near the cathode–electrolyte interface. Zhou et al.[18] used neutron reflectometry to investigate the composition profile along the depth direction near the interface at the nanometer scale, while multiple studies used electron energy-loss spectroscopy (EELS) of scanning transmission electron microscopy (STEM).[11,21,22] Although STEM EELS can be used to map Li distribution

at the tens of nanometers scale, the Li signal accounts for less than 1% of the incident electrons, so a large electron dose is required to achieve a satisfactory signal-to-noise ratio (SNR). Other groups have used STEM to obtain atomic-resolution images near the interface.[13,23] STEM imaging has enabled the visualization of light elements such as Li by annular/optimized bright-field imaging[24,25] and ptychography,[26,27] but its contrast is sensitive to the focus position, sample tilt, and sample thickness. Moreover, scanning with the electron beam induces spurious image distortions that limit the field of view to ~50 × 50 nm^2.[28] In addition, a scan step of ~30 pm is necessary to obtain atomic-resolution STEM images, which increases electron dose.[29] Such large electron doses damage metal oxides because their poor electron conductivity causes local charge accumulation, which leads to bond breaking, Coulomb explosions, and heating. Thus, an alternative visualization technique is needed that combines three key capabilities: (i) spatial resolution approaching 1 nm, (ii) a field of view spanning several hundred nanometers to enable direct comparison between interfacial and bulk regions, and (iii) low electron dose conditions to minimize sample damage.

Scanning nanobeam electron diffraction (SNED) records diffraction patterns at each probe position using a pixelated detector capable of a sub-millisecond frame rate, generating a four-dimensional (4D) dataset containing real- and reciprocal-space-resolved information.[30,31] The electron dose and scan step can be flexibly adjusted for the structural analysis of beam-sensitive materials.[32–36] SNED utilizes an aperture to narrow the beam diameter to ~1 nm, but this results in a diffraction pattern of disk-like diffraction spots on the back focal plane. Each diffraction disk exhibits a distinctive pattern that is sensitive to the sample thickness and tilt from the incident beam due to multiple scattering of electrons. Reducing the dose to avoid damaging the

sample degrades the SNR of the diffraction patterns, which makes it difficult to analyze the crystal structure.[37] To address these issues, Padgett et al. introduced cepstral analysis,[38] which was originally invented for audio signal processing.[39] Similar to the Patterson map, the cepstrum (more precisely, the amplitude cepstrum) exhibits spots corresponding to the periodicity of atomic correlations in the projected plane. Although multiple scattering exists, the diffraction pattern is approximately determined by the convolution of the structural factor, which is obtained from the crystal structure, and the observation function, which is related to experimental conditions such as the sample thickness, tilt, and bend. Therefore, the cepstrum, obtained as the amplitude of the Fourier transform of the logarithm of the diffraction pattern, additively separates the crystal structure information from the experimental conditions. Structural information can be observed more clearly in the cepstrum than in the Patterson map, which enables high-precision strain mapping[38] and structural similarity mapping within the experimental dataset.[40]

In this study, we applied cepstral matching analysis to SNED data to visualize nanoscale phase transitions at the cathode–electrolyte interface of an epitaxial $LiCoO_2$ cathode. Each experimental cepstrum was matched to cepstra simulated for the expected structural models. The epitaxial $LiCoO_2$ cathode was analyzed after 100 charge–discharge cycles up to 4.5 V. While the bulk part remained predominantly in the layered phase, spinel- and rock salt-type phases were visualized within a few nanometers of the cathode–electrolyte interface. The analysis enabled us to map the crystal phase at a spatial resolution of 1.5 nm, over a field of view several hundred nanometers across, while minimizing the influence of experimental conditions, including beam-induced damage, sample thickness, tilt, and bending.

Epitaxial $LiCoO_2$ cathodes were grown on a strontium ruthenium oxide ($SrRuO_3$) current collector that in turn was on a strontium titanium oxide ($SrTiO_3$)(111) substrate. This substrate provides only two in-plane variants, such that $LiCoO_2[100]$ or $LiCoO_2[\bar{1}00]$ is parallel to $SrTiO_3[\bar{1}10]$, thereby simplifying the subsequent analysis. The as-grown $LiCoO_2$ film exhibited the two in-plane variants, top (003) facet parallel to the $SrTiO_3$(111), side facets of {104}, and a layered structure (Figures S1 and S2). These structural characteristics are consistent with the previous reports.[19,20] Each cathode was assembled into a coin cell with an organic liquid electrolyte, a separator, and a Li metal anode. The cell showed typical charge–discharge curves and high cycling stability (Figure S3) within a cutoff voltage window of 3.5–4.2 V, in agreement with earlier studies.[4,5,41] For the subsequent observations, another coin cell was cycled 100 times in the cutoff voltage window of 3.5–4.5 V at 1C. Continuous cycling resulted in decreases in both discharge capacity and average discharge voltage (Figure S4), a typical phenomenon for $LiCoO_2$ cathodes operated with a liquid electrolyte.[5]

After the 100th discharge, the $LiCoO_2$ cathode was carefully removed from the cell and washed. The cross-section was then processed for SNED observation from the $LiCoO_2[100]$ or $LiCoO_2[\bar{1}00]$ orientation.[19] The convergence semiangle of the electron probe was set to ~2 mrad, which resulted in a diffraction disk with a diameter of ~4 mrad. This was sufficient to resolve the diffraction disks of $LiCoO_2$ with diffraction angles as small as ~5.4 mrad. The probe diameter was ~0.8 nm while the scan step was set to ~1.5 nm to achieve a high spatial resolution.

A diffraction pattern was obtained at each probe position, and the intensity was integrated in the annular dark-field (ADF) detector area and then mapped, as shown in Figure 1a. Here, the

$SrTiO_3$(111) substrate can be seen at the bottom while the $SrRuO_3$ current collector is on top of it. The overlying $LiCoO_2$ cathode had three domains (labeled as A, B, and C) within this field of view.

Figure 1b shows the experimental diffraction pattern obtained in domain A. The disks on the left are brighter than those on the right because the $LiCoO_2$[100] direction was slightly tilted relative to the incident beam. The diffraction pattern contains statistical noise and a diffuse background because of inelastically scattered electrons. Figure 1c presents a simulated diffraction pattern of the epitaxial $LiCoO_2$ cathode when viewed from the [100] direction, while Figure 1d shows the structural model. The arrangement of the diffraction disks closely matches between the experimental and simulated patterns. However, the disk intensities differ between the experiment and simulation, attributable to differences in the sample thickness and tilt.

Figures 1e and 1f show the cepstra obtained from the experimental and simulated diffraction patterns (Figures 1b and 1c), respectively (see Figures S5 and S6 for details).[42] Because of differences in the sample conditions, the center spots differ. Each cepstrum also has sharp spots with a periodic spacing of ~0.2–0.5 nm. The positions of these spots can be expressed as a linear combination of integer multiples of the vectors 1/2[$\bar{1}\bar{2}$0] and 1/6[122], which indicates that the spots come from the atomic correlation. The arrangements of the lattice-derived spots in the experimental and simulated cepstra show good agreement, which demonstrates how cepstral matching analysis facilitates a direct comparison.

The match between the experimental data and a given structural model was evaluated by

converting each cepstrum to polar coordinates around the center and excluding the center spot to consider the possibility of crystal rotation around the incident beam direction, as shown in Figures 1g and 1h.[43] The cross-correlation function was used to evaluate the similarity between the experimental and simulated cepstra. As shown in Figure 1i, the value of the cross-correlation coefficient depended on the rotation angle between the two cepstra.

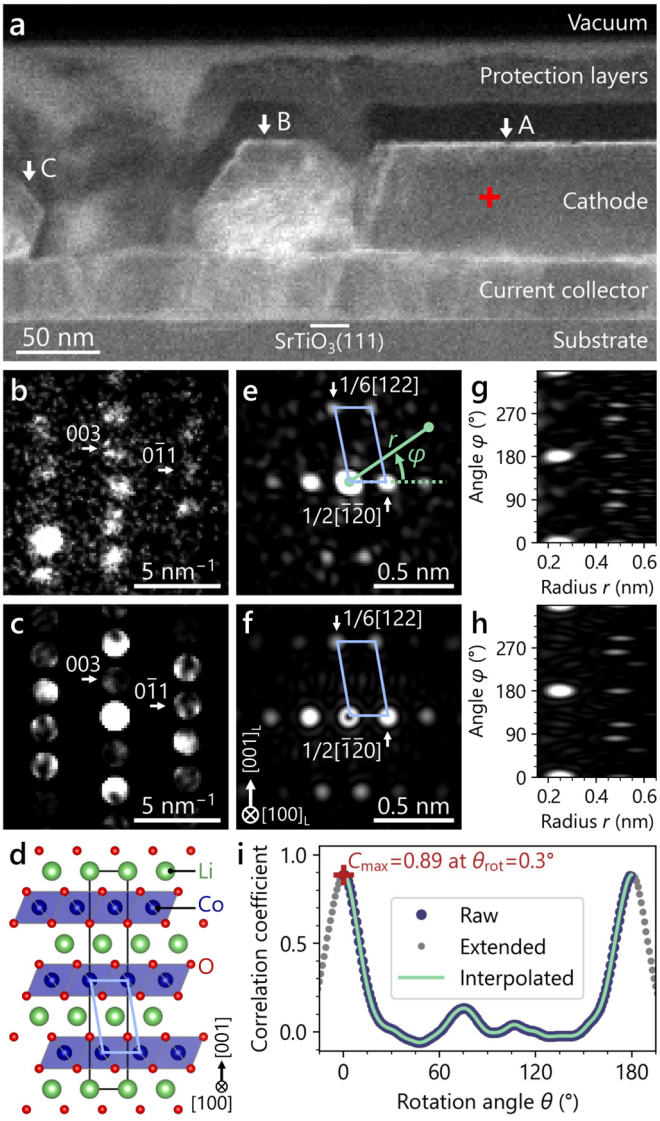


Figure 1. Visualization of the crystal phases in the epitaxial $LiCoO_2$ cathode by cepstral matching analysis. **(a)** Virtual ADF image. **(b)** Experimental diffraction pattern from the $LiCoO_2$ cathode (red cross in a) cropped for visible diffraction disks around the transmitted spot. **(c)** Diffraction pattern calculated from an atomic model of layered $LiCoO_2$, where the electron beam direction corresponds

to [100]. **(d)** Atomic model of layered $LiCoO_2$. The green, blue, and red spheres denote Li, Co, and O atoms, respectively. The black square outlines the crystallographic unit cell. Cepstra obtained from the **(e)** experimental and **(f)** simulated diffraction patterns. The blue parallelograms in d, e, and f correspond to a projected periodic pattern when viewed from the [100] direction. Polar-coordinate transforms of the **(g)** experimental and **(h)** simulated cepstra. **(i)** Cross-correlation profile comparing g and h. The raw profile (blue markers) was evaluated at 1° increments. After periodic extension (gray markers), the cubic polynomial interpolation curve (green line) was evaluated to obtain the peak position (red cross) with an accuracy of 0.1°. Because of the twofold rotational symmetry of the cepstrum, θ was defined in the range $0° \leq \theta < 180°$.

The correlation coefficient reached its maximum (C_{max}) when the experimental cepstrum most closely matched the simulated cepstrum. We mapped C_{max} across the field of view to visualize the $LiCoO_2$ cathode, as shown in Figure 2a. The $SrTiO_3$ region also exhibits a finite C_{max} value, likely due to the matching of certain spots in the cepstrum (see also Figures S7 and S8). The $LiCoO_2$ cathode region, which has a higher number of common spots between the experimental and simulated cepstra, is expected to exhibit a higher C_{max} value. By setting the lower display limit as the 75th percentile of the C_{max} values (Figure 2b), almost only the $LiCoO_2$ region becomes visible (Figure 2c). Note that although $LiCoO_2[\bar{1}00]$ is also expected from the epitaxial relationship, such a domain was not observed in this field of view (Figures S8 and S9).

Domain A exhibited a uniformly high C_{max} value (Figure 2c). Low C_{max} values were aligned along a line on the left side, which corresponded to a phase transition as described later. Domain B also showed high C_{max} values but had two parallel lines with low C_{max} values, which may correspond to shear strain (Figures S8 and S10). Domain C showed relatively low C_{max} values due to a different phase, as described later. The field of view spanned ~330 nm horizontally, allowing the visualization of both the bulk and interface parts of each domain.

The in-plane rotation angle of the cepstrum at which C_{max} occurred was denoted as θ_{rot}, and mapped in Figure 2d. θ_{rot} was uniform within domains A–C, which confirmed that each domain is a single crystal. Domains A and C had $\theta_{rot} \sim 0°$, which indicates that their [001] axes lay normal to the $SrTiO_3$(111) substrate. In contrast, domain B had $\theta_{rot} \sim 120°$, which indicates that it was rotated counterclockwise around the incident beam axis and implies a nonepitaxial relation. Supporting discussions of the maps are provided in Supporting Information (see also Figures S8–S12).

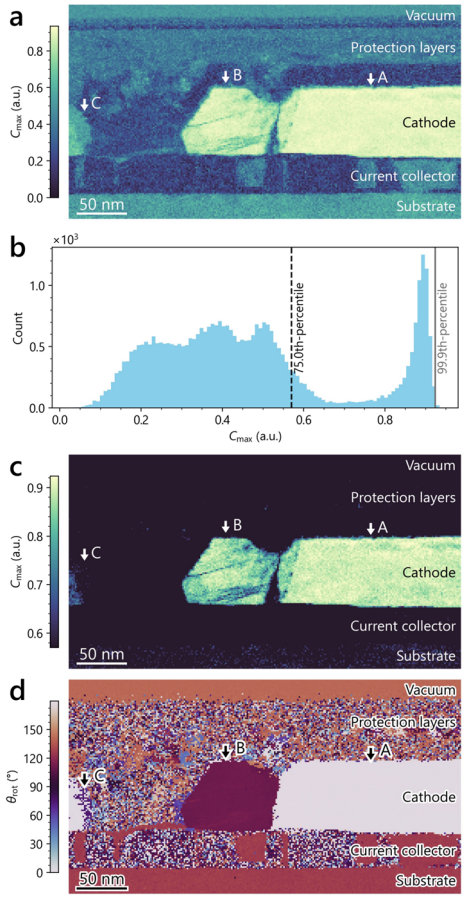


Figure 2. Maps obtained via cepstral matching analysis against simulated layered $LiCoO_2$ patterns. **(a)** Map of the maximum correlation coefficient (C_{max}). Higher values indicate greater similarity between the experimental and simulated cepstra. **(b)** Histogram of C_{max} values. The vertical lines indicate the 75th and 99.9th percentiles, shown as black dashed and gray solid lines, respectively. **(c)** C_{max} map with display range adjusted between the 75th and 99.9th percentiles. **(d)** Map of the

rotation angle (θ_{rot}) at which C_{max} was achieved. Because of the twofold rotational symmetry of the cepstrum, θ_{rot} was defined in the range of $0° \leq \theta_{rot} < 180°$.

We applied cepstral matching analysis to visualize the locations of individual spinel- and rock salt-type phases. Candidate spinel-type phases (i.e., (Li, Co)$_3O_4$, $LiCo_2O_4$, and quasi-spinel $LiCoO_2$) shared almost identical symmetry and lattice constants, which made them indistinguishable in the cepstral matching analysis (Figure S13). Therefore, they were treated as a single spinel-type phase. Figures 3a and 3b show the rock salt (CoO) and spinel (Co_3O_4) models, respectively. The models were oriented so that their CoO_6 octahedra frameworks matched those of the layered $LiCoO_2$. Figures 3c and 3d show the cepstra of these two models, respectively. Although both the rock salt- and spinel-type models belong to the cubic family, because their unit-cell sizes differed by a factor of ~2, the cepstra of these models reflected short- and long-distance atomic correlations, respectively. Compared with the cepstrum of the layered $LiCoO_2$ (Figure 1f), the rock salt cepstrum showed the presence of additional spots, whereas the spinel cepstrum showed the absence of certain spots. Therefore, the three phases could be distinguished from the cepstrum at each probe position.

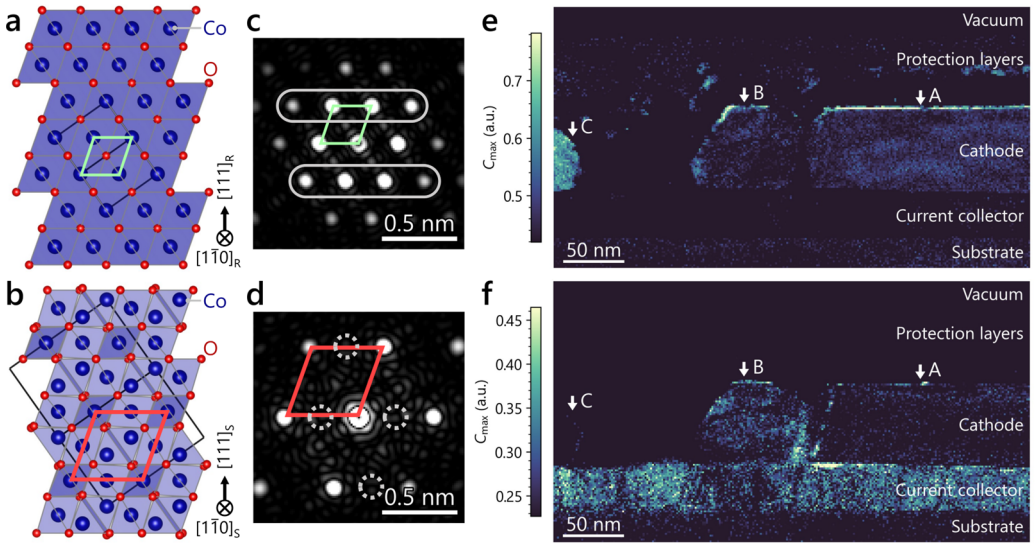


Figure 3. Atomic models, cepstra, and C_{max} maps for the rock salt CoO and spinel Co_3O_4 phases. Atomic models of **(a)** rock salt CoO and **(b)** spinel Co_3O_4. The blue and red spheres denote Co and O atoms, respectively. The subscripts R and S accompanying the Miller indices indicate rock salt and spinel phases, respectively. Simulated cepstra of the **(c)** rock salt and **(d)** spinel models. Gray dotted round rectangles in (c) and gray dotted circles in (d) highlight spots whose arrangement differs from that of the layered cepstrum in Figure 1f. The green rhombuses in (a) and (c) correspond to a projected periodic pattern of the rock salt structure when viewed from the [1-10] direction. The red rhombuses in (b) and (d) correspond to a projected periodic pattern of the spinel structure when viewed from the [1-10] direction. C_{max} maps for the simulated **(e)** rock salt and **(f)** spinel cepstra after 75th-percentile thresholding.

Figures 3e and 3f show the C_{max} maps of the rock salt- and spinel-types (see also Figure S14), respectively. The interfaces of Domains A and B exhibit a strong contrast, which will be discussed below. Within domains A and B, weak rock salt and spinel contrasts are observed, but the corresponding cepstra do not show clear spots (Figures S15 and S16). Domain C exhibits uniformly strong rock-salt contrast; however, as it differs from the other domains, a detailed discussion is beyond the scope of this work. Contrast is also seen in the protective layer, in overlap regions between domains, and in the current-collector region. Although these are not rock salt and/or spinel phases, they appear as areas with a high apparent C_{max}, as detailed in the Supporting Information. As discussed below, the appropriate interpretation and

processing of such uncertain C_{max} remain topics for future work.

Figure 4 shows a Red-Green-Blue composite of the C_{max} maps for the three phases. Hereafter, to identify the cathode interfaces that were in contact with the electrolyte during charge–discharge cycling, we denote facets using the layered-structure Miller indices with a subscript L. In Domain A, the top ~2 nm at the $(003)_L$ facet transformed into the rock salt-type phase, whereas the bulk remained almost uniformly layered. Similarly, in Domain B, the top ~3 nm at the top $(0\bar{1}4)_L$ facet was a rock salt-type phase. The top of the $(012)_L$ facet also transformed into a rock salt-type phase with a thickness of ~1 nm. In Domain B, the rock salt-type phase was thicker for the $(0\bar{1}4)_L$ and $(012)_L$ facets than for $(003)_L$. The $(003)_L$ facet is not a Li-ion intercalation/deintercalation facet, yet a weak rock salt contrast is still observed. Spinel-type contrast was observed at $(012)_L$ and part of $(003)_L$ in Domain A, and at $(012)_L$ in Domain B. These results are supported by single-point cepstra (Figures S17 and S18) and atomic-resolution STEM observations (Figures S19 and S20). They demonstrate that our cepstral matching analysis enables qualitative mapping of the crystal phase of the cathode at the electrolyte interface.

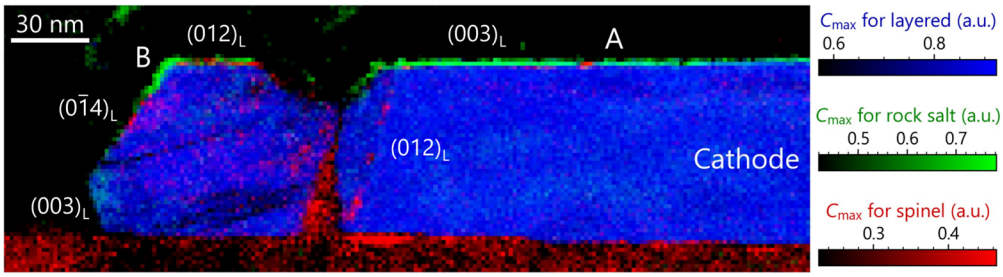


Figure 4. Red-Green-Blue composite map of C_{max} for layered (blue), rock salt (green), and spinel (red) around Domains A and B in the cathode. Higher channel intensity indicates a larger C_{max}

within the threshold range. The subscripts L accompanying the Miller indices indicate a layered structure.

Prior studies using EELS and X-ray absorption spectroscopy have shown that $LiCoO_2$ cathodes charged to ≥4.7 V result in the formation of Co_3O_4-type and CoO-type phases at the interface.[11,44] Calorimetry and gas analyses also showed that the deintercalated $Li_{0.5}CoO_2$ drives phase transitions involving oxygen release.[9,10,45,46] Ceder and Van Der Ven conducted density functional theory calculations that indicated a thermodynamic preference for the spinel phase over the layered phase in $Li_{0.5}CoO_2$.[47] Our results showed that the bulk part maintained the layered phase, whereas the cathode–electrolyte interface was transformed into rock salt- and spinel-type phases that impede Li-ion intercalation and deintercalation. Our results agree with previous studies on the phase transitions of $LiCoO_2$ at the cathode–electrolyte interface.

Compared with other STEM techniques, SNED enables less sample damage because measurements can be made at extremely low electron doses. SNED requires a total electron dose of ~3.0×10^3 $e^- nm^{-2}$,[48] which is much lower than the damage threshold of ~10^7 $e^- nm^{-2}$ for layered cathodes.[49] The $LiCoO_2$ cathode near the cathode–electrolyte interface probably contained lattice strain that was attributed to the phase transitions, and the low electron dose avoided damaging the weak structure. The electron dose for atomic-resolution STEM is ≥2.6×10^5 $e^- nm^{-2}$,[25–27] and the electron dose for EELS is ≥5×10^5 $e^- nm^{-2}$.[21] In contrast, the electron dose for SNED is lower by approximately two orders of magnitude. SNED also benefits from a large depth of focus (~1.3 μm), which exceeded the typical sample thickness by over an order of magnitude. The cepstral transformation mitigated artifacts caused by the sample thickness, tilt, and bend due to multiple scattering. These features make cepstral matching analysis

suitable for operando observations of epitaxial cathodes during charge–discharge cycles, which require time-series acquisition from the same sample region.[21,22,50]

Cepstral matching analysis is particularly effective for epitaxial films. In polycrystalline cathodes, numerous projection orientations are randomly present. Accurate mapping requires many simulated cepstra and high-SNR experimental cepstra; however, the latter necessitates a higher electron dose.[31] In electrochemical studies, $LiCoO_2${104}/$SrTiO_3$(100) epitaxial films are frequently used because $LiCoO_2${104} interfaces, which serve as Li-ion intercalation/deintercalation facets, are relatively large.[17,18,51] Our method remains applicable to such films (Figure S21), although the four in-plane variants complicate the analysis.[19,20] Even in epitaxial cathodes, the analysis cannot visualize domains whose orientations are not related by the in-plane rotations of the simulated cepstrum. This can be advantageous: excluding such minor domains yields interpretations consistent with the charge–discharge characteristics. More generally, most cathode materials are analyzable because degradation and changes in Li concentration drive symmetry-changing phase transitions,[1,2,50,52] thereby producing the presence or absence of certain cepstral spots.[38] In contrast, some phase transitions preserve the crystal symmetry while only changing the lattice constants;[41] these are not currently analyzable by our method. Taken together, these indicate that the cepstral matching analysis is particularly effective for epitaxial cathodes with predictable phase transitions involving symmetry changes.

Future challenges lie in improving the reliability and adaptability of the analysis. More advanced data processing will be needed to suppress uncertain contrast in C_{max} maps.

Systematic experiments and/or calculations should quantify the dependence of C_{max} on the phase overlap along the projection direction and evaluate how SNR, thickness, and tilt affect the accuracy. Furthermore, analyzing the cepstral spot positions yields the lattice spacings.[38] This enables mapping of symmetry-preserving transitions that change only lattice constants and of Li-ion concentration, since lattice spacings in most cathode materials vary with Li-ion concentration.[4,41] The proposed method is an important first step toward reliable, broadly applicable crystal phase analysis.

Recent research has indicated that the phase transitions of $LiCoO_2$ cathodes are reduced by doping[53] and protective coatings.[5] In addition, Ito et al.[17] reported that combining layered $LiCoO_2$ cathodes with solid electrolytes does not result in interfacial phase transitions but instead bulk phase transitions into H1–3 ($Li_{0.2}CoO_2$) and O1 (CoO_2) phases during deintercalation. Such insights emphasize the importance of visualizing phase transitions at both the interface and bulk of various cathode materials, including doped or coated $LiCoO_2$, substituted Li(Co, Mn, Ni, Al)O_2, and Li-excess layered metal oxides, at the nanoscale. Our cepstral matching analysis is a powerful tool for analyzing the crystal phase in such epitaxial cathodes at the nanoscale, which is valuable for improving the performance of rechargeable LIBs.

ASSOCIATED CONTENT

Data Availability Statement

The minimal analysis scripts supporting this study are openly available on GitHub at

https://github.com/Aso-K/cepstrum-matching-SNED. The datasets used in this study have been deposited in Zenodo at DOI:10.5281/zenodo.17007146.

Supporting Information

Supporting Information is available free of charge at …

Methods, supporting results, supporting discussion, and supporting figures (PDF)

AUTHOR INFORMATION

Corresponding Authors

TM: MASUDA.Takuya@nims.go.jp

MH: hirayama@mct.isct.ac.jp

YO: oshima@jaist.ac.jp

Notes

The authors have no competing financial interests to declare.

ACKNOWLEDGMENTS

This study was partly supported by JSPS KAKENHI (Grant Numbers JP22K14473, JP25K18108, and JP24H00042); JST GteX Program Japan (Grant Numbers JPMJGX23S5 and JPMJGX23S6); a Grant-in-Aid from the Advanced Low Carbon Technology Research and Development Program (ALCA) of JST; the Joint Research Hub Program of National Institute for Materials Science (NIMS), the Mitani Foundation for Research and Development; the Shibuya Science Culture and Sports Foundation; the Iketani Science and Technology

Foundation; the Research Foundation for the Electrotechnology of Chubu (REFEC); the Asahi Glass Foundation, and Japan Advanced Institute of Science and Technology (JAIST) Research Grant (Fundamental Research). This work was performed at the NIMS Battery Research Platform. This work was partly conducted in JAIST supported by the Advanced Research Infrastructure for Materials and Nanotechnology in Japan (ARIM) program of MEXT (JPMXP1222JI0007, JPMXP1223JI0012, and JPMXP1224JI0005).

REFERENCES

(1) Lin, C.; Li, J.; Yin, Z.; Huang, W.; Zhao, Q.; Weng, Q.; Liu, Q.; Sun, J.; Chen, G.; Pan, F. Structural Understanding for High-Voltage Stabilization of Lithium Cobalt Oxide. *Advanced Materials* **2024**, *36* (6), 2307404. https://doi.org/10.1002/adma.202307404.

(2) Lyu, Y.; Wu, X.; Wang, K.; Feng, Z.; Cheng, T.; Liu, Y.; Wang, M.; Chen, R.; Xu, L.; Zhou, J.; Lu, Y.; Guo, B. An Overview on the Advances of $LiCoO_2$ Cathodes for Lithium-Ion Batteries. *Advanced Energy Materials* **2021**, *11* (2), 2000982. https://doi.org/10.1002/aenm.202000982.

(3) Mizushima, K.; Jones, P. C.; Wiseman, P. J.; Goodenough, J. B. Li_xCoO_2 ($0<x\leq1$) A New Cathode Material for Batteries of High Energy Density. *Materials Research Bulletin* **1980**, *15* (6), 783–789. https://doi.org/10.1016/0025-5408(80)90012-4.

(4) Amatucci, G. G.; Tarascon, J. M.; Klein, L. C. CoO_2, The End Member of the Li_xCoO_2 Solid Solution. *J. Electrochem. Soc.* **1996**, *143* (3), 1114–1123. https://doi.org/10.1149/1.1836594.

(5) Yano, A.; Shikano, M.; Ueda, A.; Sakaebe, H.; Ogumi, Z. $LiCoO_2$ Degradation Behavior in the High-Voltage Phase Transition Region and Improved Reversibility with Surface Coating. *J. Electrochem. Soc.* **2017**, *164* (1), A6116–A6122. https://doi.org/10.1149/2.0181701jes.

(6) Yazami, R.; Ozawa, Y.; Gabrisch, H.; Fultz, B. Mechanism of Electrochemical Performance Decay in $LiCoO_2$ Aged at High Voltage. *Electrochimica Acta* **2004**, *50* (2–3), 385–390. https://doi.org/10.1016/j.electacta.2004.03.048.

(7) Gabrisch, H.; Yazami, R.; Fultz, B. Hexagonal to Cubic Spinel Transformation in Lithiated Cobalt Oxide. *J. Electrochem. Soc.* **2004**, *151* (6), A891. https://doi.org/10.1149/1.1738677.

(8) Wang, H.; Jang, Y.; Huang, B.; Sadoway, D. R.; Chiang, Y. TEM Study of Electrochemical Cycling-Induced Damage and Disorder in $LiCoO_2$ Cathodes for

Rechargeable Lithium Batteries. *J. Electrochem. Soc.* **1999**, *146* (2), 473–480. https://doi.org/10.1149/1.1391631.

(9) MacNeil, D. D.; Dahn, J. R. The Reaction of Charged Cathodes with Nonaqueous Solvents and Electrolytes: I. $Li_{0.5}CoO_2$. *J. Electrochem. Soc.* **2001**, *148* (11), A1205. https://doi.org/10.1149/1.1407245.

(10) MacNeil, D. D.; Dahn, J. R. The Reactions of $Li_{0.5}CoO_2$ with Nonaqueous Solvents at Elevated Temperatures. *J. Electrochem. Soc.* **2002**, *149* (7), A912. https://doi.org/10.1149/1.1483865.

(11) Kikkawa, J.; Terada, S.; Gunji, A.; Nagai, T.; Kurashima, K.; Kimoto, K. Chemical States of Overcharged $LiCoO_2$ Particle Surfaces and Interiors Observed Using Electron Energy-Loss Spectroscopy. *J. Phys. Chem. C* **2015**, *119* (28), 15823–15830. https://doi.org/10.1021/acs.jpcc.5b02303.

(12) Samarakoon, W.; Hu, J.; Song, M.; Bowden, M.; Lahiri, N.; Liu, J.; Wang, L.; Droubay, T.; Koirala, K.; Zhou, H.; Feng, Z.; Tao, J.; Du, Y. Direct Imaging of the Structural and Morphological Evolution of Epitaxial $LiCoO_2$ Films during Charge and Overcharge. *J. Phys. Chem. C* **2022**, *126* (37), 15882–15890. https://doi.org/10.1021/acs.jpcc.2c01940.

(13) Tan, H.; Takeuchi, S.; Bharathi, K. K.; Takeuchi, I.; Bendersky, L. A. Microscopy Study of Structural Evolution in Epitaxial $LiCoO_2$ Positive Electrode Films during Electrochemical Cycling. *ACS Appl. Mater. Interfaces* **2016**, *8* (10), 6727–6735. https://doi.org/10.1021/acsami.5b12025.

(14) Zhu, Y.; Wu, D.; Yang, X.; Zeng, L.; Zhang, J.; Chen, D.; Wang, B.; Gu, M. Microscopic Investigation of Crack and Strain of $LiCoO_2$ Cathode Cycled under High Voltage. *Energy Storage Materials* **2023**, *60*, 102828. https://doi.org/10.1016/j.ensm.2023.102828.

(15) Ohnishi, T.; Mitsuishi, K.; Takada, K. In Situ X-Ray Diffraction of $LiCoO_2$ in Thin-Film Batteries under High-Voltage Charging. *ACS Appl. Energy Mater.* **2021**, *4* (12), 14372–14379. https://doi.org/10.1021/acsaem.1c03046.

(16) Hikima, K.; Hinuma, Y.; Shimizu, K.; Suzuki, K.; Taminato, S.; Hirayama, M.; Masuda, T.; Tamura, K.; Kanno, R. Reactions of the Li_2MnO_3 Cathode in an All-Solid-State Thin-Film Battery during Cycling. *ACS Appl. Mater. Interfaces* **2021**, *13* (6), 7650–7663. https://doi.org/10.1021/acsami.0c18030.

(17) Ito, K.; Tamura, K.; Shimizu, K.; Yamada, N. L.; Watanabe, K.; Suzuki, K.; Kanno, R.; Hirayama, M. Degradation of a Lithium Cobalt Oxide Cathode under High Voltage Operation at an Interface with an Oxide Solid Electrolyte. *RSC Appl. Interfaces* **2024**, *1* (4), 790–799. https://doi.org/10.1039/D3LF00251A.

(18) Zhou, H.; Izumi, J.; Asano, S.; Ito, K.; Watanabe, K.; Suzuki, K.; Nemoto, F.; Yamada, N. L.; Aso, K.; Oshima, Y.; Kanno, R.; Hirayama, M. Fast Lithium Intercalation Mechanism on Surface-Modified Cathodes for Lithium-Ion Batteries. *Advanced Energy Materials* **2023**, *13* (44), 2302402. https://doi.org/10.1002/aenm.202302402.

(19) Nishio, K.; Ohnishi, T.; Akatsuka, K.; Takada, K. Crystal Orientation of Epitaxial $LiCoO_2$ Films Grown on $SrTiO_3$ Substrates. *Journal of Power Sources* **2014**, *247*, 687–691. https://doi.org/10.1016/j.jpowsour.2013.08.132.

(20) Li, Z.; Yasui, S.; Takeuchi, S.; Creuziger, A.; Maruyama, S.; Herzing, A. A.; Takeuchi, I.; Bendersky, L. A. Structural Study of Epitaxial $LiCoO_2$ Films Grown by Pulsed Laser Deposition on Single Crystal $SrTiO_3$ Substrates. *Thin Solid Films* **2016**, *612*, 472–482. https://doi.org/10.1016/j.tsf.2016.05.017.

(21) Nomura, Y.; Yamamoto, K.; Kuwata, N.; Hirayama, T. Imaging Phase Boundary Kinetics in Lithium Titanate Using Operando Electron Energy-Loss Spectroscopy. *ACS Energy Lett.* **2025**, *10* (3), 1404–1410. https://doi.org/10.1021/acsenergylett.5c00209.

(22) Nomura, Y.; Yamamoto, K.; Fujii, M.; Hirayama, T.; Igaki, E.; Saitoh, K. Dynamic Imaging of Lithium in Solid-State Batteries by Operando Electron Energy-Loss Spectroscopy with Sparse Coding. *Nature Communications* **2020**, *11* (1), 2824. https://doi.org/10.1038/s41467-020-16622-w.

(23) Ikuhara, Y. H.; Gao, X.; Kawahara, K.; Fisher, C. A. J.; Kuwabara, A.; Ishikawa, R.; Moriwake, H.; Ikuhara, Y. Atomic-Level Changes during Electrochemical Cycling of Oriented $LiMn_2O_4$ Cathodic Thin Films. *ACS Appl. Mater. Interfaces* **2022**, *14* (5), 6507–6517. https://doi.org/10.1021/acsami.1c18630.

(24) Oshima, Y.; Sawada, H.; Hosokawa, F.; Okunishi, E.; Kaneyama, T.; Kondo, Y.; Niitaka, S.; Takagi, H.; Tanishiro, Y.; Takayanagi, K. Direct Imaging of Lithium Atoms in LiV_2O_4 by Spherical Aberration-Corrected Electron Microscopy. *Microscopy* **2010**, *59* (6), 457–461. https://doi.org/10.1093/jmicro/dfq017.

(25) Ooe, K.; Seki, T.; Ikuhara, Y.; Shibata, N. Ultra-High Contrast STEM Imaging for Segmented/Pixelated Detectors by Maximizing the Signal-to-Noise Ratio. *Ultramicroscopy* **2021**, *220*, 113133. https://doi.org/10.1016/j.ultramic.2020.113133.

(26) Wang, Z.; Hu, X.; Zhang, Y.; Wu, X.; Shi, H.; Liu, W.; Yu, Y. Ptychographic Observation of Lithium Atoms in the Irradiation-Sensitive Garnet-Type Solid Electrolyte at Sub-Angstrom Resolution. *J. Am. Chem. Soc.* **2025**, *147* (21), 18025–18032. https://doi.org/10.1021/jacs.5c03627.

(27) Mitsuishi, K.; Nakazawa, K.; Sagawa, R.; Shimizu, M.; Matsumoto, H.; Shima, H.; Takewaki, T. Direct Observation of Cu in High-Silica Chabazite Zeolite by Electron Ptychography Using Wigner Distribution Deconvolution. *Sci Rep* **2023**, *13* (1), 316. https://doi.org/10.1038/s41598-023-27452-3.

(28) Aso, K.; Maebe, J.; Tran, X. Q.; Yamamoto, T.; Oshima, Y.; Matsumura, S. Subpercent Local Strains Due to the Shapes of Gold Nanorods Revealed by Data-Driven Analysis. *ACS Nano* **2021**, *15* (7), 12077–12085. https://doi.org/10.1021/acsnano.1c03413.

(29) Jiang, N. Electron Beam Damage in Oxides: A Review. *Rep. Prog. Phys.* **2016**, *79* (1), 016501. https://doi.org/10.1088/0034-4885/79/1/016501.

(30) Ophus, C. Four-Dimensional Scanning Transmission Electron Microscopy (4D-STEM): From Scanning Nanodiffraction to Ptychography and Beyond. *Microscopy and Microanalysis* **2019**, No. 2019, 563–582. https://doi.org/10.1017/S1431927619000497.

(31) Diebold, A. C.; Ophus, C.; Kordijazi, A.; Consiglio, S.; Lombardo, S.; Triyoso, D.; Tapily, K.; Mian, A.; Shankar, N. B. V. I.; Morávek, T.; Chandran, N.; Stroud, R.; Leusink, G. Template Matching Approach for Automated Determination of Crystal Phase and Orientation of Grains in 4D-STEM Precession Electron Diffraction Data for Hafnium Zirconium Oxide Ferroelectric Thin Films. *Microscopy and Microanalysis* **2025**, *31* (2), ozaf019. https://doi.org/10.1093/mam/ozaf019.

(32) Wang, Z.; Zhai, W.; Yu, Y. Revealing the Distribution of Lithium Compounds in Lithium Dendrites by Four-Dimensional Electron Microscopy Analysis. *Nano Lett.* **2024**, *24* (8), 2537–2543. https://doi.org/10.1021/acs.nanolett.3c04537.

(33) Hau, H.-M.; Mishra, T.; Ophus, C.; Huang, T.-Y.; Bustilo, K.; Sun, Y.; Yang, X.; Holstun, T.; Zhao, X.; Wang, S.; Ha, Y.; Lee, G.-H.; Song, C.; Turner, J.; Bai, J.; Ma, L.; Chen, K.; Wang, F.; Yang, W.; McCloskey, B. D.; Cai, Z.; Ceder, G. Earth-Abundant Li-Ion Cathode Materials with Nanoengineered Microstructures. *Nat. Nanotechnol.* **2024**, *19* (12), 1831–1839. https://doi.org/10.1038/s41565-024-01787-y.

(34) Chen, W.; Zhan, X.; Yuan, R.; Pidaparthy, S.; Yong, A. X. B.; An, H.; Tang, Z.; Yin, K.; Patra, A.; Jeong, H.; Zhang, C.; Ta, K.; Riedel, Z. W.; Stephens, R. M.; Shoemaker, D. P.; Yang, H.; Gewirth, A. A.; Braun, P. V.; Ertekin, E.; Zuo, J.-M.; Chen, Q. Formation and Impact of Nanoscopic Oriented Phase Domains in Electrochemical Crystalline Electrodes. *Nat. Mater.* **2023**, *22* (1), 92–99. https://doi.org/10.1038/s41563-022-01381-4.

(35) Han, Y.; Nguyen, K.; Cao, M.; Cueva, P.; Xie, S.; Tate, M. W.; Purohit, P.; Gruner, S. M.; Park, J.; Muller, D. A. Strain Mapping of Two-Dimensional Heterostructures with Subpicometer Precision. *Nano Lett.* **2018**, *18* (6), 3746–3751. https://doi.org/10.1021/acs.nanolett.8b00952.

(36) Chatterjee, D.; Huang, S.; Gu, K.; Ju, J.; Yu, J.; Bock, H.; Yu, L.; Ediger, M. D.; Voyles, P. M. Using 4D STEM to Probe Mesoscale Order in Molecular Glass Films Prepared by Physical Vapor Deposition. *Nano Lett.* **2023**, *23* (5), 2009–2015. https://doi.org/10.1021/acs.nanolett.3c00197.

(37) Wu, L.; Han, M.-G.; Zhu, Y. Toward Accurate Measurement of Electromagnetic Field by Retrieving and Refining the Center Position of Non-Uniform Diffraction Disks in Lorentz 4D-STEM. *Ultramicroscopy* **2023**, *250*, 113745. https://doi.org/10.1016/j.ultramic.2023.113745.

(38) Padgett, E.; Holtz, M. E.; Cueva, P.; Shao, Y.-T.; Langenberg, E.; Schlom, D. G.; Muller, D. A. The Exit-Wave Power-Cepstrum Transform for Scanning Nanobeam Electron Diffraction: Robust Strain Mapping at Subnanometer Resolution and Subpicometer

Precision. *Ultramicroscopy* **2020**, *214*, 112994. https://doi.org/10.1016/j.ultramic.2020.112994.

(39) Noll, A. M. Cepstrum Pitch Determination. *The Journal of the Acoustical Society of America* **1967**, *41* (2), 293–309. https://doi.org/10.1121/1.1910339.

(40) Yoo, T.; Hershkovitz, E.; Yang, Y.; da Cruz Gallo, F.; Manuel, M. V.; Kim, H. Unsupervised Machine Learning and Cepstral Analysis with 4D-STEM for Characterizing Complex Microstructures of Metallic Alloys. *npj Comput Mater* **2024**, *10* (1), 1–10. https://doi.org/10.1038/s41524-024-01414-3.

(41) Ohzuku, T.; Ueda, A. Solid-State Redox Reactions of $LiCoO_2$ (R-3m) for 4 Volt Secondary Lithium Cells. *J. Electrochem. Soc.* **1994**, *141* (11), 2972–2977. https://doi.org/10.1149/1.2059267.

(42) Aso, K.; Higashimine, K.; Miyata, M.; Kamio, H.; Oshima, Y. Three-Dimensional Atomic-Scale Characterization of Titanium Oxyhydroxide Nanoparticles by Data-Driven Lattice Correlation Analysis. *Commun Chem* **2025**, *8* (1), 122. https://doi.org/10.1038/s42004-025-01513-2.

(43) Kimoto, K.; Kikkawa, J.; Harano, K.; Cretu, O.; Shibazaki, Y.; Uesugi, F. Unsupervised Machine Learning Combined with 4D Scanning Transmission Electron Microscopy for Bimodal Nanostructural Analysis. *Sci Rep* **2024**, *14* (1), 2901. https://doi.org/10.1038/s41598-024-53289-5.

(44) Takamatsu, D.; Koyama, Y.; Orikasa, Y.; Mori, S.; Nakatsutsumi, T.; Hirano, T.; Tanida, H.; Arai, H.; Uchimoto, Y.; Ogumi, Z. First In Situ Observation of the $LiCoO_2$ Electrode/Electrolyte Interface by Total-Reflection X-Ray Absorption Spectroscopy. *Angewandte Chemie International Edition* **2012**, *51* (46), 11597–11601. https://doi.org/10.1002/anie.201203910.

(45) Gupta, R.; Manthiram, A. Chemical Extraction of Lithium from Layered $LiCoO_2$. *Journal of Solid State Chemistry* **1996**, *121* (2), 483–491. https://doi.org/10.1006/jssc.1996.0067.

(46) Chebiam, R. V.; Kannan, A. M.; Prado, F.; Manthiram, A. Comparison of the Chemical Stability of the High Energy Density Cathodes of Lithium-Ion Batteries. *Electrochemistry Communications* **2001**, *3* (11), 624–627. https://doi.org/10.1016/S1388-2481(01)00232-6.

(47) Ceder, G.; Van Der Ven, A. Phase Diagrams of Lithium Transition Metal Oxides: Investigations from First Principles. *Electrochimica Acta* **1999**, *45* (1–2), 131–150. https://doi.org/10.1016/S0013-4686(99)00199-1.

(48) Egerton, R. F. Dose Measurement in the TEM and STEM. *Ultramicroscopy* **2021**, *229*, 113363. https://doi.org/10.1016/j.ultramic.2021.113363.

(49) Seo, J. H.; Na, S.; Ahn, S. J.; Park, K.; Lee, S.; Lee, J.; Kwon, J.-H. Electron Beam-Induced Effects on a Ni-Rich Layered Cathode Material: A Comprehensive Investigation Using STEM and EELS. *J. Phys. Chem. C* **2024**, *128* (22), 9099–9104.

https://doi.org/10.1021/acs.jpcc.4c00600.

(50) Lee, S.; Oshima, Y.; Hosono, E.; Zhou, H.; Kim, K.; Chang, H. M.; Kanno, R.; Takayanagi, K. Phase Transitions in a $LiMn_2O_4$ Nanowire Battery Observed by Operando Electron Microscopy. *ACS Nano* **2015**, *9* (1), 626–632. https://doi.org/10.1021/nn505952k.

(51) Takeuchi, S.; Tan, H.; Bharathi, K. K.; Stafford, G. R.; Shin, J.; Yasui, S.; Takeuchi, I.; Bendersky, L. A. Epitaxial $LiCoO_2$ Films as a Model System for Fundamental Electrochemical Studies of Positive Electrodes. *ACS Appl. Mater. Interfaces* **2015**, *7* (15), 7901–7911. https://doi.org/10.1021/am508512q.

(52) Hess, M.; Sasaki, T.; Villevieille, C.; Novák, P. Combined Operando X-Ray Diffraction–Electrochemical Impedance Spectroscopy Detecting Solid Solution Reactions of $LiFePO_4$ in Batteries. *Nat Commun* **2015**, *6* (1), 8169. https://doi.org/10.1038/ncomms9169.

(53) Yoon, M.; Dong, Y.; Yoo, Y.; Myeong, S.; Hwang, J.; Kim, J.; Choi, S.-H.; Sung, J.; Kang, S. J.; Li, J.; Cho, J. Unveiling Nickel Chemistry in Stabilizing High-Voltage Cobalt-Rich Cathodes for Lithium-Ion Batteries. *Advanced Functional Materials* **2020**, *30* (6), 1907903. https://doi.org/10.1002/adfm.201907903.

Table of Contents Image

